

Theory for shear displacement by light-induced Raman force in bilayer graphene

Habib Rostami *

Nordita, KTH Royal Institute of Technology and Stockholm University, Hannes Alfvéns väg 12, 10691 Stockholm, Sweden

 (Received 1 May 2022; revised 28 August 2022; accepted 22 September 2022; published 10 October 2022)

Coherent excitation of shear phonons in van der Waals layered materials is a nondestructive mechanism to fine-tune the lattice structure and the electronic state of the system. We develop a diagrammatic theory for the displacive Raman force and apply it to the shear phonon's dynamics. We obtain a noticeable light-induced Raman force of the order of $\mathcal{F} \sim 10\text{--}100$ nN/nm² leading to a large rectified shear displacement Q_0 in bilayer graphene. In analogy to the photogalvanic effect, we decompose the Raman force to circular and linear components where the former vanishes due to the lattice symmetry in bilayer graphene. We show that the laser frequency and polarization can effectively tune Q_0 in different electronic doping, temperature, and scattering rates. The finite rectified shear displacement induces a Dirac crossing pair in the low-energy dispersion that photoemission spectroscopy can probe. Our systematic formalism of Raman force can simulate the coherent manipulation of stacking order in the heterostructures of layered materials by laser irradiation.

DOI: [10.1103/PhysRevB.106.155405](https://doi.org/10.1103/PhysRevB.106.155405)

I. INTRODUCTION

In van der Waals (vdW) layered materials, e.g., the family of graphene and transition-metal dichalcogenides (TMDs), the stacking order of layers is crucial for the ground-state characteristic features. The physical properties of an AB stack bilayer graphene [A-sublattice on top of B-sublattice; see Fig. 1(a)] are different from that of an AA-stack one [1–8]. In trilayer graphene, two common structures are with ABA and ABC stacking with and without a center of symmetry, respectively [9–15]. In twisted two-dimensional (2D) materials with an asymmetric layer rotation, e.g., twisted bilayer and trilayer graphene [4,16–20], the ground state depends strongly on the twist due to the flat-band formation at magic twist angles [4,21,22]. The relative lateral layer shift in a small twist-angle incommensurate bilayer, with a large moiré lattice constant, can be gauged away by a unitary transformation [4]. However, its impact is significant for a large twist-angle. A rigid relative displacement along the armchair direction by one C-C bond length $a_0 \sim 0.14$ nm or a 60° relative layer twist can switch between AA and AB prototypes. The relative lateral displacement of top and bottom layers versus the middle one in twisted trilayer graphene can drastically change the density of states and superconducting critical temperature [15,23,24]. Although there is a surge of interest in twisted multilayers, the impact of the relative lateral shift in vdW layered materials is

less highlighted in the literature. This work aims to fill that gap.

Shear phonons in vdW layered materials correspond to the lateral asymmetric sliding of atomic layers [25–33]. The doubly degenerate Raman-active shear mode in bilayer graphene has a soft frequency $\hbar\Omega_0 \approx 3.9$ meV [25] due to the weak vdW interlayer coupling. In trilayer there are two doubly degenerate modes: Raman-active ≈ 3.9 meV and infrared-active 4.7 meV [25]. The stimulated Raman effect is an efficient mechanism to excite Raman-active vibrational modes [34,35]. The photoinduced structural transition in layered quantum materials such as multilayer graphene, WTe₂, and MoTe₂ is rapidly evolving using the ultrafast pump-probe setup and time-resolved second-harmonic-generation spectroscopy [36–40]. Shear phonon dynamics can manipulate the stacking order of layers [38,40] and the electronic topology [37]. A displacive coherent excitation of the Raman-active shear phonon in MoTe₂ causes a first-order phase transition from inversion symmetric $1T'$ structure to the noncentrosymmetric $1T_d$ phase [38,39]. A structural phase switch from ABA to ABC stacking is experimentally obtained by laser irradiation on trilayer graphene [36]. Many physical phenomena, such as optical switching of polar metals, moiré ferroelectrics, and superconductivity, are directly correlated to the shear phonon dynamics in the heterostructures of layered quantum materials [15,41–47]. The relatively low frequency of shear phonons makes them highly susceptible to displace significantly under a light-induced Raman force.

In this paper, we study coherent shear phonon dynamics employing a diagrammatic framework in vdW layered materials. Collective macroscopic oscillation of atoms in a crystalline solid, i.e., coherent phonons, facilitates a nondestructive control [48,49] of physical properties by irradiating ultrashort laser pulses and employing transient optical spectroscopy [50–61]. We provide a theory for the *displacive Raman force* (DRF), and we implement it to excite coherent

*habib.rostami@su.se

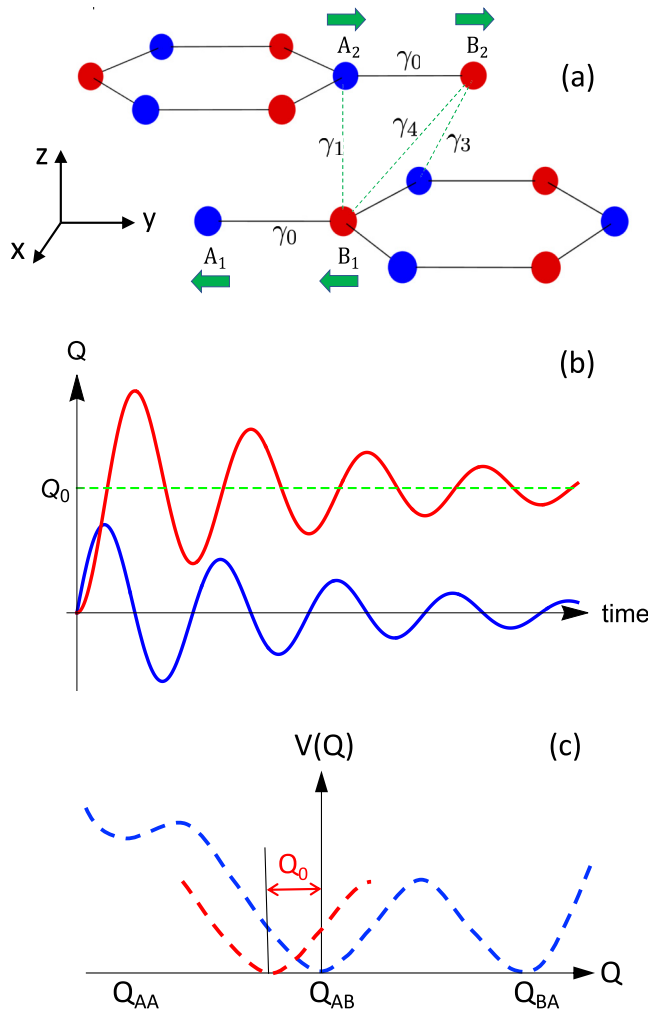


FIG. 1. Schematic of coherent shear phonon in bilayer graphene. (a) The y -component of shear phonon mode in bilayer graphene. We illustrate the fundamental hopping mechanism in bilayer graphene denoted by γ_i 's. The intralayer carbon-carbon bond length is $a_0 \approx 0.14$ nm, the interlayer distance is $c \approx 0.34$ nm, and the bond length for γ_3 and γ_4 hoppings is given by $b = \sqrt{c^2 + a_0^2} \approx 0.38$ nm. Hopping parameters are given as $\gamma_0 \approx 3$ eV, $\gamma_1 \approx -0.4$ eV, $\gamma_3 \approx 0.3$ eV, and $\gamma_4 \approx 0.1$ eV [7]. (b) Impulsive (blue curve) and displaceive (red curve) coherent phonon. (c) Schematic of the lattice potential $V(Q)$ in bilayer graphene vs displacement field along an armchair (y -axis) direction. Starting from the stable AB stack phase at $Q_{AB} = 0$, we can achieve the equivalent BA stacking phase or the metastable AA structure by sliding the top layer to the right or left, respectively. The light-induced shear displacement is depicted by Q_0 .

shear phonons in bilayer graphene (BLG). The excitation of coherent shear modes can change the electronic structure and trigger a structural transition to another quasiequilibrium state. We obtain highly efficient tunability of Raman force by altering electronic doping and temperature as well as laser frequency, polarization, and power. The harmonic equation of motion for the coherent phonon displacement \mathbf{Q} reads

$$\partial_t^2 \mathbf{Q}(t) + \Omega_0^2 \mathbf{Q}(t) = \mathcal{F}(t)/\rho, \quad (1)$$

where ρ stands for the mass density of the 2D material, and $\mathcal{F}(t)$ is the light-induced force density.

For an ultrashort δ -function pulse, the Raman force density can have impulsive $\mathcal{F}^I(t) \sim \mathcal{F}\delta(t)$ and displaceive $\mathcal{F}^D(t) \sim \mathcal{F}\Theta(t)$ characters where $\Theta(t) = \int_{-\infty}^t dt' \delta(t')$ is the Heaviside step function [55,59–61]. The impulsive force leads to the coherent vibration of ions around equilibrium positions, while under a displaceive force ions shift away from the equilibrium positions to a new local equilibrium and then vibrate around the new equilibrium positions [see Fig. 1(b)]. The real and imaginary parts of the Raman susceptibility contribute to the impulsive and displaceive forces, respectively [59–61]. For the laser frequency larger than the optical transition edge, the imaginary part is finite and thus DRF is nonzero [61]. In what follows, we evaluate DRF and demonstrate its relevance for the light-induced shear displacement in BLG.

II. MODEL

The dipole moment of the Raman-active phonon $\mu_a = \alpha_{ab}E_b$ is linearly proportional to the light electric field E_b where the polarizability tensor α_{ab} depends on the phonon displacement vector \mathbf{Q} . The electromagnetic potential energy then yields $U = -\mu_a E_a = -\alpha_{ab}E_a E_b$. The corresponding Raman force thus reads $F_c = -\partial U/\partial Q_c = \sigma_{abc}^R E_a E_b$ with the Raman susceptibility $\sigma_{abc}^R = \partial \alpha_{ab}/\partial Q_c|_{Q \rightarrow 0}$ [34,35]. We adopt Einstein convention for summation on repeated indices. Although the lowest-order Raman effect is a second-order nonlinear optical process, it does not require an inversion symmetry breaking. This is because the Raman-active mode in a centrosymmetric system is even under parity [35].

The displaceive (rectified) force will displace ions to a new equilibrium position $\mathbf{Q}_0 \approx \mathcal{F}^D/(\rho\Omega_0^2)$. Then ions vibrate around the new equilibrium with the phonon frequency Ω_0 ; see Fig. 1. Apparently, the rigid displacement is more pronounced for the soft shear phonons with shallow frequency relative to other energy scales such as temperature and electronic chemical potential. The displaceive force is governed by the rectification process $\mathcal{F}_a^D \sim \int dt \mathcal{F}_a(t)$, and it is given by

$$\mathcal{F}_a^D = \sigma_{abc}^R(\omega, -\omega) E_b(\omega) E_c^*(\omega), \quad (2)$$

where ω is the light frequency and σ_{abc}^R is the Raman response function that is the correlation function of electron-phonon and light-matter couplings.

Having the in-plane displacement $\mathbf{Q}^{(\ell)}(\mathbf{r})$ of two layers $\ell = 1, 2$, the shear phonon displacement is the asymmetric component:

$$\mathbf{Q} = \frac{\mathbf{Q}^{(1)} - \mathbf{Q}^{(2)}}{\sqrt{2}}. \quad (3)$$

The shear displacement vector is even under parity \mathcal{P} since $\mathcal{P}\{\mathbf{Q}^{(1)}, \mathbf{Q}^{(2)}\}\mathcal{P}^{-1} = -\{\mathbf{Q}^{(2)}, \mathbf{Q}^{(1)}\}$, which leads to $\mathcal{P}\mathbf{Q}\mathcal{P}^{-1} = \mathbf{Q}$. Therefore, it is a Raman-active and IR-inactive phonon. The second quantized form of the shear phonon displacement reads $\hat{Q}_{\lambda,\mathbf{q}} = \sqrt{\hbar/\rho S \Omega_{\lambda,\mathbf{q}}} (\hat{b}_{\lambda,\mathbf{q}} + \hat{b}_{\lambda,-\mathbf{q}}^\dagger)$, where λ indicates two Cartesian components $\lambda = x, y$. We recall boson statistics $[\hat{b}_{\lambda,\mathbf{q}}, \hat{b}_{\lambda',\mathbf{q}'}^\dagger] = \delta_{\lambda\lambda'} \delta_{\mathbf{q}\mathbf{q}'}$ and $[\hat{b}_{\lambda,\mathbf{q}}, \hat{b}_{\lambda',\mathbf{q}'}] = 0$. Note that S is the 2D material area. The leading Hamiltonian of finite- \mathbf{q} phonon

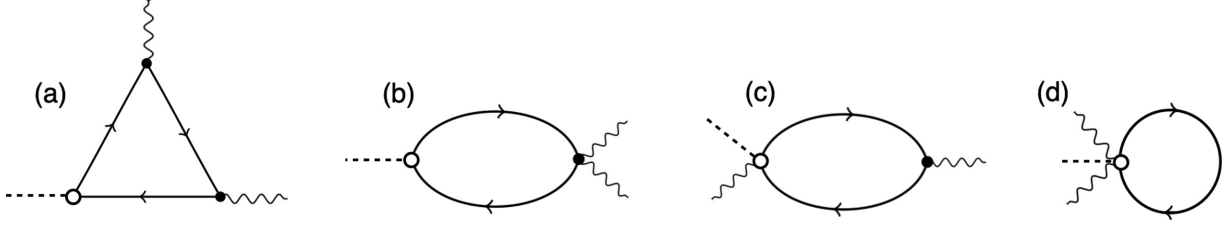


FIG. 2. Feynman diagrams for Raman force. Dashed and wavy lines represent external phonon and photon fields, respectively. The solid lines represent electron propagators.

$\hat{b}_{\lambda,\mathbf{q}}$ interacting with electron spinor fields $\hat{\Psi}_{\mathbf{k}}$ is given by

$$\hat{\mathcal{H}} = \sum_{\mathbf{k}} \hat{\Psi}_{\mathbf{k}}^\dagger \hat{H}_{\mathbf{k}} \hat{\Psi}_{\mathbf{k}} + \sum_{\lambda,\mathbf{q}} \hbar \Omega_{\lambda,\mathbf{q}} \hat{b}_{\lambda,\mathbf{q}}^\dagger \hat{b}_{\lambda,\mathbf{q}} + \sum_{\mathbf{k},\mathbf{q}} \sum_{\lambda} \hat{\Psi}_{\mathbf{k}+\mathbf{q}}^\dagger \hat{g}_{\lambda}(\mathbf{k}, \mathbf{q}) \hat{\Psi}_{\mathbf{k}} (\hat{b}_{\lambda,\mathbf{q}} + \hat{b}_{\lambda,-\mathbf{q}}^\dagger), \quad (4)$$

where the electron-phonon coupling is given in terms of the matrix-element \hat{M}_{λ} as

$$\hat{g}_{\lambda}(\mathbf{k}, \mathbf{q}) = \sqrt{\frac{\hbar}{2\rho S \Omega_{\lambda,\mathbf{q}}}} \hat{M}_{\lambda}(\mathbf{k}, \mathbf{q}). \quad (5)$$

The hermiticity of the Hamiltonian implies that $\hat{M}_{\lambda}^\dagger(\mathbf{k} + \mathbf{q}, -\mathbf{q}) = \hat{M}_{\lambda}(\mathbf{k}, \mathbf{q})$. Using the Heisenberg time-evolution relation $\langle \partial_t \hat{b}_{\lambda,\mathbf{q}} \rangle = (i/\hbar) \langle [\hat{\mathcal{H}}, \hat{b}_{\lambda,\mathbf{q}}] \rangle$, we arrive at the classical equation of motion for the coherent phonon $\mathcal{Q}_{\lambda,\mathbf{q}}(t) = \langle \hat{\mathcal{Q}}_{\lambda,\mathbf{q}} \rangle$. The coherent phonon equation motion follows Eq. (1) for $\mathbf{q} = \mathbf{0}$. The Raman force density is given as the expectation value of the electron-phonon coupling

$$\mathcal{F}_{\lambda,\mathbf{q}}(t) = -\frac{1}{S} \sum_{\mathbf{k}} \langle \hat{\Psi}_{\mathbf{k}-\mathbf{q}}^\dagger \hat{M}_{\lambda}(\mathbf{k}, -\mathbf{q}) \hat{\Psi}_{\mathbf{k}} \rangle \quad (6)$$

that is related to the excitation density if \hat{M}_{λ} is proportional to the identity matrix; see also Ref. [58]. In general, the force is given as the expectation value of the electron-phonon matrix element that can be written in a perturbative expansion in terms of the light electric field [62]. The light-induced electron density generates a force acting on ions. For the normal incidence of light, only the $\mathbf{q} = \mathbf{0}$ phonon is Raman-active.

The light-matter coupling is incorporate by minimal coupling transformation $\hbar\mathbf{k} \rightarrow \hbar\mathbf{k} + e\mathbf{A}(t)$ using a homogeneous dynamical vector potential $\mathbf{A}(t)$. The corresponding electric field reads $\mathbf{E}(t) = -\partial_t \mathbf{A}(t)$. The light-matter interaction consists of photon-electron and photon-electron-phonon coupling terms:

$$\mathcal{H}_{lm} = - \sum_{\mathbf{k}} \hat{\Psi}_{\mathbf{k}}^\dagger \left\{ \hat{j}_a A_a(t) + \frac{1}{2} \hat{\gamma}_{ab} A_a(t) A_b(t) + \hat{\Theta}_{ab} A_a(t) Q_b(t) + \frac{1}{2} \hat{\Delta}_{abc} A_a(t) A_b(t) Q_c(t) \right\} \hat{\Psi}_{\mathbf{k}}, \quad (7)$$

where $\hat{j}_a(\mathbf{k})$ is called the paramagnetic current operator and $\hat{\gamma}_{ab}(\mathbf{k})$ is known as the diamagnetic current operator as well as the Raman vertex in the effective-mass approximation [63]. The photon-electron-phonon interaction couplings are parametrized by $\hat{\Theta}_{ab}(\mathbf{k})$ and $\hat{\Delta}_{abc}(\mathbf{k})$. The photon-electron-phonon couplings originate from the minimal

coupling transformation in the electron-phonon matrix element $\hat{M}_{\lambda}(\mathbf{k} + e\mathbf{A}(t)/\hbar, \mathbf{q})$ and then expanding it up to second order in the light field. We follow the standard many-body perturbation theory and utilize a diagrammatic framework [64–67]. Accordingly, the Raman force response function σ_{abc}^R consists of four diagrams, as shown in Fig. 2. Having defined the key aspects of the model, we calculate DRF and the resulting shear displacement in bilayer graphene.

III. SHEAR PHONON IN BILAYER GRAPHENE

Bilayer graphene consists of two single layers of graphene sheets offset from each other in the xy -plane. The low-energy quasiparticles in BLG follow a two-band Hamiltonian around the corners of the hexagonal Brillouin zone [68],

$$\hat{H}_{\mathbf{p}} = -\frac{1}{2m} \{ (p_x^2 - p_y^2) \hat{\sigma}_x + 2\tau p_x p_y \hat{\sigma}_y \} - \mu \hat{I}, \quad (8)$$

where $\mathbf{p} = \hbar\mathbf{k}$ is the momentum vector, $\tau = \pm$ stands for two K and K' valley points, the identity matrix \hat{I} and Pauli matrices $\hat{\sigma}_{x,y}$ are in the layer pseudospin basis, and μ is the chemical potential. The x -direction indicates a zigzag orientation of the hexagonal crystal in our convention [69]. The effective mass is given by $1/2m \approx v^2/\gamma_1$ with $v = 3\gamma_0 a_0/2\hbar \sim 10^6$ m/s. Note that γ_i 's are hopping energies in the lattice model illustrated in Fig. 1(a), and their numerical values are given in the caption. We neglect trigonal warping and effective mass asymmetry in the energy dispersion of chiral fermions in BLG. In pristine BLG, two degenerate shear modes correspond to the sliding motion in two Cartesian directions.

To evaluate the Raman force, we consider electron-photon couplings $\hat{j}_\alpha = -e\partial_{p_\alpha} \hat{H}_{\mathbf{p}}$ and $\hat{\gamma}_{\alpha\beta} = -e^2 \partial_{p_\alpha} \partial_{p_\beta} \hat{H}_{\mathbf{p}}$. In the low-energy model, the couplings of electrons to shear phonons are given by (see Appendix A)

$$(\hat{M}_x, \hat{M}_y) \approx M(\tau \hat{\sigma}_y, \hat{\sigma}_x),$$

$$(\hat{\Theta}_{xy} = \hat{\Theta}_{yx}, \hat{\Theta}_{yy} = -\hat{\Theta}_{xx}) \approx -\Theta(\tau \hat{\sigma}_x, \hat{\sigma}_y). \quad (9)$$

The electron-phonon couplings are obtained using a four-band tight-binding model following the approach presented in Refs. [70–72]—we refer to Appendix A for the detailed derivation and discussion on electrons coupling to shear phonons in BLG. After neglecting electron momentum p , we obtain (see Appendix A)

$$M = \gamma_3 \frac{3a_0}{\sqrt{2}b^2} \beta_3,$$

$$\Theta = \frac{e\gamma_3}{\hbar} \frac{3a_0^2}{2\sqrt{2}b^2} \beta_3 = \frac{ea_0}{2\hbar} M, \quad (10)$$

where $\beta_3 = -\partial \ln \gamma_3 / \partial \ln b$ is a Grüneisen parameter, and $b = \sqrt{c^2 + a_0^2}$ with $c \approx 0.34$ nm and $a_0 = 0.14$ nm are the interlayer distance and the intralayer bond length, respectively. An *ab initio* analysis based on the density functional calculation estimates the dependence of γ_3 on the bond length as $\partial \gamma_3 / \partial b \approx -0.54$ eV/Å [71] and therefore one can obtain the Grüneisen parameter $\beta_3 = -(b/\gamma_3)\partial \gamma_3 / \partial b \approx 6.84$. The vertical hopping derivative $\partial \gamma_1 / \partial c$ does not contribute to the leading-order electron-phonon interaction.

IV. RESULTS AND DISCUSSION

In analogy to the linear and circular photogalvanic current [73], we decompose the Raman force density into linear and circular components (see Appendix B):

$$\begin{aligned} \mathcal{F}_a^{\text{LDR}} &= \gamma_{abc}^{\text{LDR}}(\omega) \text{Re}[E_b(\omega)E_c^*(\omega)], \\ \mathcal{F}_a^{\text{CDR}} &= \gamma_a^{\text{CDR}}(\omega)[i\mathbf{E}(\omega) \times \mathbf{E}^*(\omega)]_z. \end{aligned} \quad (11)$$

For an electric field polarization in the xy -plane, the linear displacive Raman (LDR) and circular displacive Raman (CDR) response functions read (see Appendix B)

$$\begin{aligned} \gamma_{abc}^{\text{LDR}}(\omega) &= \text{Re}[\sigma_{abc}^{\text{R}}(\omega, -\omega)], \\ \gamma_a^{\text{CDR}}(\omega) &= \text{Im}[\sigma_{axy}^{\text{R}}(\omega, -\omega)]. \end{aligned} \quad (12)$$

A generic elliptical polarization of the incident laser field $\mathbf{E}(t) = E_0\{\cos(\vartheta)\hat{\mathbf{x}} \pm i\sin(\vartheta)\hat{\mathbf{y}}\}e^{-i\omega t}$ contains both linear and circular counterparts: $[i\mathbf{E}(\omega) \times \mathbf{E}^*(\omega)]_z = \pm \sin(2\vartheta)$ and $\text{Re}[E_b(\omega)E_c^*(\omega)] = \delta_{ab}(\delta_{ax}\cos^2\vartheta + \delta_{ay}\sin^2\vartheta)$. Considering the inversion and rotational symmetries of the low-energy model, we find nonvanishing real-valued tensor elements

$$\sigma_{yyy}^{\text{R}} = \sigma_{xxy}^{\text{R}} = \sigma_{xyx}^{\text{R}} = -\sigma_{yxx}^{\text{R}}, \quad (13)$$

where we have dropped the frequency argument $\sigma_{abc}^{\text{R}}(\omega, -\omega)$ for the sake of shorthand notation. Accordingly, the symmetry implies that σ_{axy}^{R} is either zero ($a = y$) or real-valued ($a = x$) leading to a vanishing circular DRF in BLG: $\mathcal{F}^{\text{CDR}} = 0$. To have the CDR force finite, we need to break rotational symmetry for instance by applying a uniaxial strain. Furthermore, considering the nonvanishing matrix elements of σ_{abc}^{R} given in Eq. (13), we can easily obtain the LDR force contribution in response to an elliptically polarized incident laser, which reads

$$\mathcal{F}^{\text{LDR}} = -\hat{y}\mathcal{F}_0\Lambda(\bar{\omega}_1, \bar{\omega}_2)\cos(2\vartheta). \quad (14)$$

Therefore, the Raman force vanishes for a circularly polarized light $\vartheta = \pm\pi/4$. Note that $\mathcal{F}_0 = N_f M (eE_0)^2 / (4\pi\mu^2)$ with $N_f = 4$ for spin-valley degeneracy. For $\mu = 0.2$ eV and $E_0 = 1$ V/nm, we obtain the force density unit $\mathcal{F}_0 \approx 2.3$ nN/nm². For linear polarized incident light $\mathbf{E}(t) = E_0\{\cos(\theta)\hat{\mathbf{x}} + \sin(\theta)\hat{\mathbf{y}}\}e^{-i\omega t}$, the Raman force follows:

$$\mathcal{F}^{\text{LDR}} = \mathcal{F}_0\Lambda(\bar{\omega}_1, \bar{\omega}_2)\{\sin(2\theta)\hat{\mathbf{x}} - \cos(2\theta)\hat{\mathbf{y}}\}, \quad (15)$$

where the force vector is not necessarily parallel to the driving electric field. In Fig. 3(a), the Raman force orientation is compared to the incident laser polarization. The frequency dependence of the Raman force is captured by the dimensionless function $\Lambda(\bar{\omega}_1, \bar{\omega}_2)$. There are topologically

distinct contributions to the Raman force, which are illustrated diagrammatically in Fig. 2. Using Kubo's formalism, we analytically calculate Raman response functions at zero electronic temperature (see Appendix C),

$$\begin{aligned} \Lambda(\bar{\omega}_1, \bar{\omega}_2) &= \frac{\bar{\omega}_1 + 2\bar{\omega}_2}{(\bar{\omega}_1 + \bar{\omega}_2)\bar{\omega}_2^2} \ln \left[\frac{4 - \bar{\omega}_1^2}{4 - (\bar{\omega}_1 + \bar{\omega}_2)^2} \right] \\ &+ \frac{\bar{\omega}_2 + 2\bar{\omega}_1}{(\bar{\omega}_1 + \bar{\omega}_2)\bar{\omega}_1^2} \ln \left[\frac{4 - \bar{\omega}_2^2}{4 - (\bar{\omega}_1 + \bar{\omega}_2)^2} \right] \\ &- \frac{3}{2\bar{\omega}_1\bar{\omega}_2} \ln \left[1 - \frac{(\bar{\omega}_1 + \bar{\omega}_2)^2}{4} \right]. \end{aligned} \quad (16)$$

Notice that $\bar{\omega}_j = (\hbar\omega_j + i\Gamma_e)/|\mu|$, where Γ_e stands for the phenomenological scattering rate of electrons. The above expression stems from the triangular diagram and a bubble diagram shown in Figs. 2(a) and 2(b), respectively. The contribution from the Feynman diagram depicted in Fig. 2(c) vanishes within the low-energy model analysis. The last diagram shown in Fig. 2(d) is frequency-independent, and its value is fixed by enforcing the gauge invariance where the response to a static homogeneous gauge potential must vanish due to the gauge invariance, i.e., $\chi_{abc}^{\text{R}}(0, 0) = 0$. For the displacive force, we set $\omega_1 = -\omega_2 = \omega$ and therefore it scales as $\mathcal{F}^{\text{D}} \sim 1/\Gamma_e$. In Fig. 3(b), we illustrate the magnitude of DRF versus frequency $\hbar\omega/|\mu|$ for different values of phenomenological scattering rate Γ_e . The displacive force is finite in the interband regime $\hbar\omega > 2|\mu|$, and at the large frequency, the force density scales as $\mathcal{F}^{\text{D}} = 2M(eE_0)^2/(\pi\hbar\omega\Gamma_e)$.

Due to the electron-electron scatterings, the nonequilibrium photoexcited electrons reach a quasiequilibrium condition with a high electronic temperature of the order of $T_e \sim 10^3$ – 10^4 K depending on the incident pump power and electron-phonon coupling strength [74–78]. It is worth mentioning that for a slow enough repetition rate of the pump laser, the absorbed power of the individual pulses does not add to a considerable energy accumulation to heat the lattice. Thus, even with a very high electronic temperature, the lattice will remain at the experimental temperature that can be ambient or even cryogenic. The displacive force and interband optical absorption occur coincidentally. Thus, we anticipate a quasiequilibrium hot-electron state with high electronic temperature in a metal for an intense incident laser. Using the standard Maldaque's formula (see Appendix D), we calculate the Raman force in finite electronic temperature T_e and we illustrate the results in Figs. 3(c) and 3(d), which show an enhancement of the displacive force in the intraband regime and a robust Drude-like tail emerging at low frequency. However, the interband force is diminished at finite T_e .

Using $\mathbf{Q}_0 \approx \mathcal{F}^{\text{D}}/(\rho\Omega_0^2)$ and $\rho = c\rho_{\text{gr}}$ for the mass density of BLG, with $\rho_{\text{gr}} \approx 2.267$ kg/cm³ being the three-dimensional graphite density, we estimate the strength of the displacive shear displacement as depicted in Fig. 3(d). This displacement is robust and tuneable by altering the Fermi energy, incident laser frequency, and laser intensity. We find giant values for Q_0 in our leading-order theory considering realistic experimental values for laser intensity and carrier doping. The saturation value of shear phonon displacement was measured to be around $Q_{\text{max}} \sim 8$ pm in layered WTe₂ using intense infrared laser with electric field strength

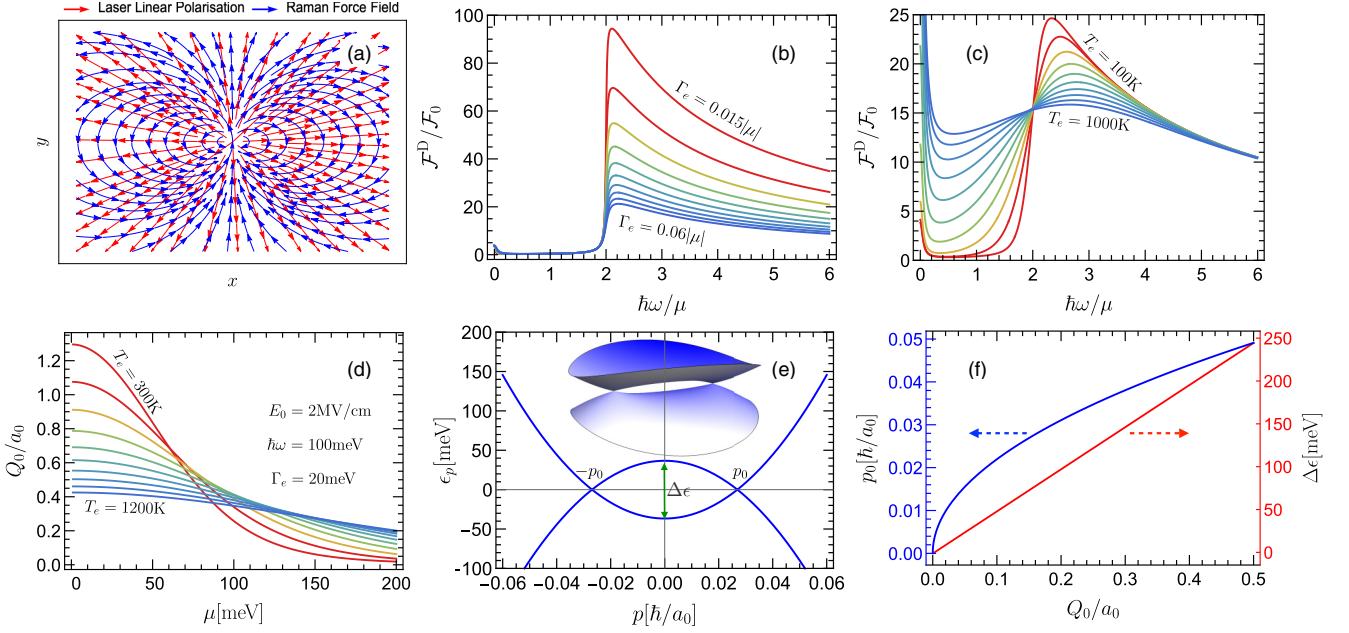


FIG. 3. Displacive Raman force and rectified shear displacement in bilayer graphene. (a) Orientation of DRF in comparison to the incident laser polarization. (b) Raman force vs the driving frequency for different values of electronic scattering rate Γ_e at zero electronic temperature $T_e = 0$. As seen, the zero-temperature Raman force is finite in the interband regime where $\hbar\omega > 2|\mu|$ and for large frequency it scales as $\mathcal{F} \sim 1/(\Gamma_e\omega)$. (c) Raman force vs the driving frequency for different values of the electronic temperature T_e at $\Gamma_e = 0.01|\mu|$. At finite temperature, the displacive force is finite even in the intraband regime $\hbar\omega < 2|\mu|$. (d) Rectified shear displacement vs chemical potential for realistic experimental values of frequency $\hbar\omega = 100$ meV, electric field strength $E_0 = 2$ MV/cm, and electron scattering rate $\Gamma_e = 20$ meV. (e) Low-energy dispersion of bilayer graphene under rigid shear displacement $Q_0 = 0.15a_0$. The original band touching at $p = 0$ is lifted, and a pair of Dirac crossings form at $\pm p_0$. The inset shows the 3D energy dispersion. (f) The band splitting $\Delta\epsilon$ at $p = 0$ and the new Dirac crossing location p_0 are tuneable by the shear displacement Q_0 as depicted in this double-sided plot.

$E_0 \sim 7.5$ MV/cm [37] and $E_0 \sim 10$ MV/cm [40]. Although the earlier experiment [37] does not support a Raman mechanism, the latter [40] measures a linear power ($P \sim E_0^2$) dependence of the shear displacement consistent with the Raman force $\mathcal{F}^D \propto E_0^2$. Such a linear power dependence is also reported in Ref. [38].

In a bilayer graphene system with the chemical potential $\mu = 200$ meV and considering the interband regime $\hbar\omega = 2\mu$, we estimate the shear displacement $Q_0 \sim 0.19a_0 \sim 27$ pm for $E_0 \sim 2$ MV/cm by setting electronic temperature $T_e = 1000$ K and scattering rate $\Gamma_e = 20$ meV. This value of Q_0 is clearly immense and motivates further experimental investigation of displacive Raman force for coherent control of stacking order in bilayer graphene and other 2D material heterostructure. In reality, the significant value of shear displacement enhances nonlinear corrections where the higher-order terms in the electric field and phonon anharmonicity give rise to the shear displacement saturation, which is observed experimentally [37]. We sketch a schematic nonlinear lattice potential versus the shear displacement in bilayer graphene in Fig. 1(c) with the stable AB (or BA) stacking phase and the metastable AA stacking structure as local minima at higher energy. Since we neglect anharmonicity, the validity range of our theory is for small enough shear displacement $Q_0 < a_0$ around the stable AB structure. Such coherent control of the lattice potential minimum can have implications for the optical switching of ferroelectricity and superconductivity in layered materials [23,47].

The rigid shear displacement (frozen shear phonon) induces a perturbation to the electronic Hamiltonian according to Eq. (4) that, for instance, at the K -point ($\tau = +$) reads $\delta\hat{H} = M(Q_{0,x}\hat{\sigma}_y + Q_{0,y}\hat{\sigma}_x)$. As a result of this frozen shear phonon, the band touching point at $p = 0$ splits by $\Delta\epsilon = 2MQ_0$ and a Dirac crossing pair forms at $\mathbf{p}_0 = \pm p_0(\cos\phi_0, \sin\phi_0)$ in the Cartesian coordinates, where we find [see Fig. 3(e)]

$$p_0 = \sqrt{2mMQ_0}, \quad \tan(2\phi_0) = Q_{0,x}/Q_{0,y}. \quad (17)$$

For linear polarized incident laser, the rectified shear displacement is $\mathbf{Q}_0 = Q_0(\sin(2\theta), -\cos(2\theta))$, with θ being the incident laser polarization angle. Therefore, we find $\phi_0 = -\theta$, which implies that the new Dirac crossing points are aligned to the incident laser polarization. The energy splitting $\Delta\epsilon$ and the position of the crossing point p_0 depend on the rigid shear displacement as illustrated in Fig. 3(f). In principle, this change in the dispersion is significant enough to be experimentally measured utilizing angle-resolved photoemission spectroscopy.

V. REMARKS AND OUTLOOK

Considering the linear absorption coefficient α , we create one photoexcited electron in the conduction band for each absorbed photon and leave a hole in the valence band. In the steady state, we have a vanishing rate of carrier density $\dot{n}(t) = I_{\text{abs}}/\hbar\omega - \delta n/\tau_e = 0$. Therefore, one can estimate the

photoexcited carrier density $\delta n = I_{\text{abs}}\tau_e/\hbar\omega$, where $I_{\text{abs}} = \alpha I_{\text{pump}}$ is the absorbed intensity in which $I_{\text{pump}} \propto E_0^2$ is the pump laser intensity and $\tau_e = \hbar/\Gamma_e$ is the electronic relaxation time. From the analytical result of the photoinduced displacive Raman force, one can notice that it is directly proportional to the photoexcited carrier density $\mathcal{F}^D \sim E_0^2/(\hbar\omega\Gamma_e) \sim \delta n$.

The timescale during which a large enough shear displacement can be induced depends on the microscopics of the materials. The displacive Raman force is finite during the recombination time that can certainly reach a picosecond depending on the magnitude of the photoexcited density, the photoexcitation energy, and the equilibrium density [75]. Exotic photoluminescence in graphene indicates an asymptotically long-lived quasiequilibrium condition of light-induced hot electrons and hot optical phonons [74]. Moreover, time-resolved differential optical transmission experiments in graphene confirm a light-induced band structure renormalization on a timescale of a few picoseconds, $\tau > 1$ ps [79–81]. The subpicosecond response of the lattice to the laser pulse is reported in different experiments (e.g., in MoTe₂ [38,39] and in diamond [54]). Therefore, the recombination timescale of photoexcited density in bilayer graphene and other van der Waals layered materials is long enough to sustain a large light-induced shear displacement.

The proposed mechanism of displacive Raman force can strongly impact the Raman-active shear phonon dynamics in twisted systems, particularly in trilayer graphene. The theory can be generalized to investigate displacive coherent dynamics of other collective modes, such as magnons [82] and superconducting Higgs mode [67], driven by a rectified light-induced force field. In future studies, we will develop a higher-order Raman force mechanism to manipulate chiral valley phonons [83,84] in hexagonal 2D materials. In a separate study, we will discuss the saturation of rigid shear displacement using a higher-order Raman force scheme. The light-induced rigid shear displacement can basically switch the ferroelectric polarization in moiré ferroelectrics [42–44] and 2D ferroelectrics (polar) metals [41,45–47]. Having an optical switch of electric polarization can have technological applications for ferroelectric memories.

ACKNOWLEDGMENTS

This work was supported by Nordita and the Swedish Research Council (VR Starting Grant No. 2018-04252). Nordita is partially supported by Nordforsk. I am grateful to E. Cappelluti, J. Weissenrieder, F. Guinea, and A. Tomadin for useful discussion and feedback.

APPENDIX A: ELECTRON COUPLING TO THE SHEAR PHONONS

We recall the four-band tight-binding model to describe the electronic Hamiltonian of electrons in bilayer graphene [7],

$$H_{\mathbf{k}} = \begin{bmatrix} \epsilon_{A_1} & -\gamma_0 f_{\mathbf{k}} & \gamma_4 f_{\mathbf{k}} & -\gamma_3 f_{\mathbf{k}}^* \\ -\gamma_0 f_{\mathbf{k}}^* & \epsilon_{B_1} & \gamma_1 & \gamma_4 f_{\mathbf{k}} \\ \gamma_4 f_{\mathbf{k}}^* & \gamma_1 & \epsilon_{A_2} & -\gamma_0 f_{\mathbf{k}} \\ -\gamma_3 f_{\mathbf{k}} & \gamma_4 f_{\mathbf{k}}^* & -\gamma_0 f_{\mathbf{k}}^* & \epsilon_{B_2} \end{bmatrix}, \quad (\text{A1})$$

where the form factor reads

$$f_{\mathbf{k}} = \sum_{\ell=1}^3 e^{i\mathbf{k}\cdot\delta_{\ell}} = e^{ia_0k_y} + 2ie^{-a_0k_y/2} \cos(\sqrt{3}a_0k_x/2). \quad (\text{A2})$$

The intralayer nearest-neighbor vectors are $\delta_1 = a_0(0, 1)$, $\delta_2 = a_0(\sqrt{3}/2, -1/2)$, and $\delta_3 = a_0(-\sqrt{3}/2, -1/2)$. Note that $a_0 \approx 0.14$ nm is the carbon-carbon bond length. The two valley points ($\tau = \pm$) are at the corner of the hexagonal Brillouin zone: $\tau\mathbf{K} = \tau \frac{4\pi}{\sqrt{3}a_0} \hat{\mathbf{x}}$. The low-energy model is obtained by momentum expansion near the valley point: $\mathbf{k} = \tau\mathbf{K} - \mathbf{q}$ for $q \ll K$, which leads to $f_{\mathbf{q}} = \frac{3a_0\gamma_0}{2}(q_x - iq_y)$. The electron-phonon coupling is obtained by considering the dependence of hopping parameters on the phonon displacement.

Shear mode vibration only affects interlayer hopping elements: γ_1 , γ_3 , and γ_4 . In this Appendix, we calculate one- and two-phonon couplings to electrons in bilayer graphene in both four- and two-band models. In the main text, we only consider the impact of one-phonon coupling. The contribution of two-phonon coupling on electrons will be discussed elsewhere.

1. Impact of shear displacement on γ_1

The shear phonon displacement Q changes the bond length corresponding to γ_1 interlayer hopping as shown in Fig. 1(b). However, this correction is second order in Q :

$$\gamma_1(\ell) = \gamma_1(c) + \frac{\partial\gamma_1}{\partial c}(\ell - c) + \dots, \quad (\text{A3})$$

where c and ℓ stand for the A2-B1 bond length in the pristine and displaced system, respectively. Therefore, we have

$$\frac{\ell - c}{c} \approx \frac{Q^2}{2c^2} \rightarrow \frac{\delta\gamma_1}{\gamma_1} \approx -\beta_1 \frac{Q^2}{2c^2}. \quad (\text{A4})$$

We define $\beta_1 = -\partial \ln \gamma_1 / \partial \ln c$. Accordingly, in the leading one-phonon-electron coupling we can neglect the impact of shear displacement on the vertical γ_1 hopping.

2. Impact of shear displacement on γ_3

The shear phonon displacement Q changes the distance of the bond corresponding to γ_3 interlayer hopping as shown in Fig. 1(b). The change in the hopping γ_3 is shown by $\delta\gamma_3$, which leads to

$$\frac{\delta\gamma_3(d_{\ell})}{\gamma_3} = \left(\frac{1}{\gamma_3} \frac{\partial\gamma_3}{\partial b} \right) \Delta d_{\ell} + \frac{1}{2} \left(\frac{1}{\gamma_3} \frac{\partial^2\gamma_3}{\partial b^2} \right) (\Delta d_{\ell})^2 + \dots \quad (\text{A5})$$

Note that $\mathbf{d}_{\ell} = \delta_{\ell} + c\hat{\mathbf{z}}$ corresponds to three A1-B2 bond lengths in the pristine system and $b = |\mathbf{d}_{\ell}| = \sqrt{c^2 + a_0^2}$. The change in the bond length then follows:

$$\Delta d_{\ell} = |\mathbf{d}_{\ell} + \mathbf{Q}_A(\mathbf{R}) - \mathbf{Q}_B(\mathbf{R} - \mathbf{d}_{\ell})| - |\mathbf{d}_{\ell}|, \quad (\text{A6})$$

in which \mathbf{Q}_A is the displacement of sublattice A in layer 1 and \mathbf{Q}_B is the displacement of sublattice B in layer 2 at the lattice

point \mathbf{R} . We define the shear displacement \mathbf{Q} as follows:

$$\mathbf{Q}_A(\mathbf{R}) - \mathbf{Q}_B(\mathbf{R} - \mathbf{d}_\ell) = \sqrt{2}\mathbf{Q}. \quad (\text{A7})$$

Therefore, the change in the bond length reads

$$\Delta d_\ell \approx \frac{\sqrt{2}\mathbf{d}_\ell \cdot \mathbf{Q}}{b}. \quad (\text{A8})$$

We find the correction $\delta\gamma_3$ up to second order in the shear displacement field \mathbf{Q} :

$$\frac{\delta\gamma_3(d_\ell)}{\gamma_3} = -\beta_3 \frac{\sqrt{2}(\boldsymbol{\delta}_\ell \cdot \mathbf{Q})}{b^2} - \kappa_3 \frac{(\boldsymbol{\delta}_\ell \cdot \mathbf{Q})^2}{b^4}, \quad (\text{A9})$$

in which we define

$$\beta_3 = -\frac{\partial \ln \gamma_3}{\partial \ln b}, \quad \kappa_3 = -\frac{b^2}{\gamma_3} \frac{\partial^2 \gamma_3}{\partial b^2}. \quad (\text{A10})$$

Accordingly, the correction to the form factor for the γ_3 hopping term reads

$$\begin{aligned} \sum_\ell \frac{\delta\gamma_3(d_\ell)}{\gamma_3} e^{i\mathbf{k} \cdot \boldsymbol{\delta}_\ell} &= -\frac{\sqrt{2}\beta_3}{b^2} \mathbf{Q} \cdot \sum_\ell \boldsymbol{\delta}_\ell e^{i\mathbf{k} \cdot \boldsymbol{\delta}_\ell} - \frac{\kappa_3}{b^4} Q_a Q_b \sum_\ell \delta_\ell^a \delta_\ell^b e^{i\mathbf{k} \cdot \boldsymbol{\delta}_\ell} \\ &= -\frac{\sqrt{2}\beta_3}{b^2} Q_a (-i\partial_{k_a}) \sum_\ell e^{i\mathbf{k} \cdot \boldsymbol{\delta}_\ell} - \frac{\kappa_3}{b^4} Q_a Q_b (-i\partial_{k_a})(-i\partial_{k_b}) \sum_\ell e^{i\mathbf{k} \cdot \boldsymbol{\delta}_\ell} \\ &= -\frac{\sqrt{2}\beta_3}{b^2} Q_a (-i\partial_{k_a}) f_{\mathbf{k}} - \frac{\kappa_3}{b^4} Q_a Q_b (-i\partial_{k_a})(-i\partial_{k_b}) f_{\mathbf{k}}, \end{aligned} \quad (\text{A11})$$

which simplifies as follows:

$$\sum_\ell \frac{\delta\gamma_3(d_\ell)}{\gamma_3} e^{i\mathbf{k} \cdot \boldsymbol{\delta}_\ell} = -\beta_3 \frac{\sqrt{2}a_0}{b^2} g_a(\mathbf{k}) Q_a - \kappa_3 \frac{a_0^2}{b^4} h_{ab}(\mathbf{k}) Q_a Q_b, \quad (\text{A12})$$

and we define

$$g_a(\mathbf{k}) = \frac{1}{a_0} (-i\partial_{k_a}) f_{\mathbf{k}}, \quad h_{ab}(\mathbf{k}) = -\frac{1}{a_0^2} \partial_{k_a} \partial_{k_b} f_{\mathbf{k}}. \quad (\text{A13})$$

3. Impact of shear phonon displacement on γ_4

Similar to the case of γ_3 , one can obtain the correction to γ_4 -related form factors as follows:

$$\sum_\ell \frac{\delta\gamma_4(d_\ell)}{\gamma_4} e^{i\mathbf{k} \cdot \boldsymbol{\delta}_\ell} = -\beta_4 \frac{\sqrt{2}a_0}{b^2} g_a(\mathbf{k}) Q_a - \kappa_4 \frac{a_0^2}{b^4} h_{ab}(\mathbf{k}) Q_a Q_b, \quad (\text{A14})$$

where

$$\beta_4 = -\frac{\partial \ln \gamma_4}{\partial \ln b}, \quad \kappa_4 = -\frac{b^2}{\gamma_4} \frac{\partial^2 \gamma_4}{\partial b^2}. \quad (\text{A15})$$

4. One shear phonon's coupling to electrons

In the four-band model, the coupling of one shear phonon to electrons can be written as follows:

$$H_{ep} = \sum_{\mathbf{k}} \sum_a \hat{\Psi}_{\mathbf{k}}^\dagger \hat{M}_a(\mathbf{k}) \hat{\Psi}_{\mathbf{k}} \hat{Q}_a, \quad (\text{A16})$$

where the electron-phonon matrix element is given by

$$\hat{M}_a(\mathbf{k}) = \begin{bmatrix} 0 & 0 & -\alpha_4 g_a(\mathbf{k}) & \alpha_3 g_a^*(\mathbf{k}) \\ 0 & 0 & 0 & -\alpha_4 g_a(\mathbf{k}) \\ -\alpha_4 g_a^*(\mathbf{k}) & 0 & 0 & 0 \\ \alpha_3 g_a(\mathbf{k}) & -\alpha_4 g_a^*(\mathbf{k}) & 0 & 0 \end{bmatrix}, \quad (\text{A17})$$

where we define $\alpha_i = (\sqrt{2}\beta_i a_0 / b^2) \gamma_i$.

5. Two shear phonons' coupling to electrons

In the four-band model, the coupling of two shear phonons to electrons reads

$$\hat{H}_{ep} = \sum_{\mathbf{k}} \sum_{ab} \hat{\Psi}_{\mathbf{k}}^\dagger \hat{W}_{ab}(\mathbf{k}) \hat{\Psi}_{\mathbf{k}} \hat{Q}_a \hat{Q}_b, \quad (\text{A18})$$

where the electron-phonon matrix element is given by

$$\hat{W}_{ab}(\mathbf{k}) = \begin{bmatrix} 0 & 0 & -\eta_4 h_{ab}(\mathbf{k}) & \eta_3 h_{ab}^*(\mathbf{k}) \\ 0 & 0 & -\eta_1 \delta_{ab} & -\eta_4 h_{ab}(\mathbf{k}) \\ -\eta_4 h_{ab}^*(\mathbf{k}) & -\eta_1 \delta_{ab} & 0 & 0 \\ \eta_3 h_{ab}(\mathbf{k}) & -\eta_4 h_{ab}^*(\mathbf{k}) & 0 & 0 \end{bmatrix}, \quad (\text{A19})$$

where we define

$$\eta_1 = \frac{\beta_1}{2c^2} \gamma_1, \quad \eta_3 = \frac{\kappa_3 a_0^2}{b^4} \gamma_3, \quad \eta_4 = \frac{\kappa_4 a_0^2}{b^4} \gamma_4. \quad (\text{A20})$$

6. Low-energy two-band model

In this subsection, we obtain a two-band model Hamiltonian for the electron couplings to shear phonons up to second order in electron momentum and phonon displacement field. We follow the effective Green's-function approach [68] to

drive to effective Hamiltonian. Consider a 4×4 Hamiltonian and Green's function written in terms of 2×2 blocks \hat{H}_{ij} and \hat{G}_{ij} :

$$\hat{H} = \begin{bmatrix} \hat{H}_{11} & \hat{H}_{12} \\ \hat{H}_{21} & \hat{H}_{22} \end{bmatrix}, \quad \hat{G} = \begin{bmatrix} \hat{G}_{11} & \hat{G}_{12} \\ \hat{G}_{21} & \hat{G}_{22} \end{bmatrix}. \quad (\text{A21})$$

Note that the Green's function is defined as $\hat{G}(\hat{E} - \hat{H}) = \hat{I}$. One can simply show

$$\hat{G}_{11}\{E - \hat{H}_{11} - \hat{H}_{12}(E - \hat{H}_{22})^{-1}\hat{H}_{21}\} = \hat{I}. \quad (\text{A22})$$

At low energy of a gapless system, we can set $E = 0$ and thus we rewrite

$$\hat{G}_{11}\{E - \hat{H}_{11} + \hat{H}_{12}\hat{H}_{22}^{-1}\hat{H}_{21}\} = \hat{G}_{11}(E - \hat{H}_{\text{eff}}) = \hat{I}, \quad (\text{A23})$$

where the effective Hamiltonian reads

$$\hat{H}_{\text{eff}} = \hat{H}_{11} - \hat{H}_{12}\hat{H}_{22}^{-1}\hat{H}_{21}. \quad (\text{A24})$$

We follow the above steps and obtain the low-energy Hamiltonian

$$\hat{H}_{\text{eff}} = \sum_{\mathbf{k}} \hat{\Psi}_{\mathbf{k}}^\dagger \left\{ \hat{H}_{\mathbf{k}} + \sum_a \hat{M}_a(\mathbf{k}) Q_a + \sum_{ab} \hat{W}_{ab}(\mathbf{k}) Q_a Q_b \right\} \hat{\Psi}_{\mathbf{k}}. \quad (\text{A25})$$

The two-band kinetic Hamiltonian thus reads

$$H_{\mathbf{q}} = -\frac{\hbar^2}{2m} \begin{bmatrix} 0 & (\tau q_x - iq_y)^2 \\ (\tau q_x + iq_y)^2 & 0 \end{bmatrix}, \quad (\text{A26})$$

$$\begin{aligned} \hat{M}_a(\mathbf{k} + e\mathbf{A}(t)/\hbar) &= \begin{bmatrix} 0 & 0 & -\alpha_4 g_a(\mathbf{k} + e\mathbf{A}(t)/\hbar) & \alpha_3 g_a^*(\mathbf{k} + e\mathbf{A}(t)/\hbar) \\ 0 & 0 & 0 & -\alpha_4 g_a(\mathbf{k} + e\mathbf{A}(t)/\hbar) \\ -\alpha_4 g_a^*(\mathbf{k} + e\mathbf{A}(t)/\hbar) & 0 & 0 & 0 \\ \alpha_3 g_a(\mathbf{k} + e\mathbf{A}(t)/\hbar) & -\alpha_4 g_a^*(\mathbf{k} + e\mathbf{A}(t)/\hbar) & 0 & 0 \end{bmatrix} \\ &\approx \frac{ea_0 A_b(t)}{\hbar} \begin{bmatrix} 0 & 0 & -i\alpha_4 h_{ab}(\mathbf{k}) & -i\alpha_3 h_{ab}^*(\mathbf{k}) \\ 0 & 0 & 0 & -i\alpha_4 h_{ab}(\mathbf{k}) \\ i\alpha_4 h_{ab}^*(\mathbf{k}) & 0 & 0 & 0 \\ i\alpha_3 h_{ab}(\mathbf{k}) & i\alpha_4 h_{ab}^*(\mathbf{k}) & 0 & 0 \end{bmatrix}. \end{aligned} \quad (\text{A31})$$

Afterward, we follow the previous section's procedure and obtain a low-energy two-band model for the above photon-mediated electron-phonon interaction in order to obtain Θ_{ab} mixed photon-electron-phonon coupling elements. At leading order in electronic momentum, we obtain the parameter Θ , which is given in Eq. (10). A similar approach can be used to obtain two-phonon-electron coupling mediated by photons starting from $\hat{W}_{ab}(\mathbf{k} + e\mathbf{A}(t)/\hbar)$.

APPENDIX B: CIRCULAR AND LINEAR DISPLACIVE RAMAN FORCE

The rectification (displacive) Raman force is obtained by setting $\omega_1 + \omega_2 = 0$. In response to a monochromatic external electric field $\mathbf{E}(t) = 2 \text{Re}[\mathbf{E}(\omega)e^{i\omega t}]$, it can be formally written as follows:

$$\mathcal{F}_a^{\text{dc}} = \sigma_{abc}^{\text{R}}(\omega, -\omega) E_b(\omega) E_c^*(\omega), \quad (\text{B1})$$

in which the effective mass is related to both intra- and inter-layer hopping energies

$$\frac{\hbar^2}{2m} = \frac{9a_0^2 \gamma_0^2}{4\gamma_1}. \quad (\text{A27})$$

The electron-phonon interaction at $\mathbf{q} = \mathbf{0}$ is given by

$$(\hat{M}_x, \hat{M}_y) = M(\tau \hat{\sigma}_y, \hat{\sigma}_x). \quad (\text{A28})$$

Accordingly, we obtain the value of the parameter M given in Eq. (10) of the main text:

$$M = \frac{3\alpha_3}{2} = \frac{3\beta_3 a_0}{\sqrt{2}b^2} \gamma_3. \quad (\text{A29})$$

Although the analysis of this manuscript does not require multiphonon couplings, we also calculate the coupling for the two-phonon-electron term at $\mathbf{q} = \mathbf{0}$, and the only nonvanishing terms are given by

$$\hat{W} = \begin{bmatrix} \hat{W}_{xx} & \hat{W}_{xy} \\ \hat{W}_{yx} & \hat{W}_{yy} \end{bmatrix} = \frac{3}{2} \left(\frac{3\alpha_4^2}{\gamma_1} - \eta_3 \right) \begin{bmatrix} \hat{\sigma}_x & \tau \hat{\sigma}_y \\ \tau \hat{\sigma}_y & -\hat{\sigma}_x \end{bmatrix}. \quad (\text{A30})$$

7. Photon-electron-phonon couplings

To calculate the mixed vertex coupling for photon-electron-phonon couplings, we start with minimal transformation $\mathbf{k} \rightarrow \mathbf{k} + e\mathbf{A}(t)/\hbar$ in the electron-phonon interaction Hamiltonian given in Eqs. (A31) and (A19). For instance, the photon-electron-phonon vertex coupling is obtained as follows:

where $\sigma_{abc}^{\text{R}}(\omega, -\omega) = \sigma_{acb}^{\text{R}}(-\omega, \omega) = \chi_{abc}^{\text{R}}(\omega, -\omega)/\omega^2$ is the gauge-invariant displacive Raman response function. The reality of the electric field in the time domain implies $\mathbf{E}(-\omega) = \mathbf{E}^*(\omega)$. We decompose linear and circular rectification processes by utilizing the following relation:

$$\begin{aligned} E_b(\omega) E_c^*(\omega) &= \frac{E_b(\omega) E_c^*(\omega) + E_c(\omega) E_b^*(\omega)}{2} \\ &\quad + \frac{E_b(\omega) E_c^*(\omega) - E_c(\omega) E_b^*(\omega)}{2} \\ &= \text{Re}[E_b(\omega) E_c^*(\omega)] + \frac{1}{2} \epsilon_{\ell bc} [\mathbf{E}(\omega) \times \mathbf{E}^*(\omega)]_{\ell}, \end{aligned} \quad (\text{B2})$$

where the first and second terms on the right side of the above relation lead to the linear and displacive Raman force, respectively. In analogous to the linear and circular photogalvanic effect [73], the Raman response function can be decomposed into symmetric and antisymmetric parts standing for the linear

and circular displacive force contributions, respectively,

$$\begin{aligned}\sigma_{abc}^R(\omega, -\omega) &= \frac{\sigma_{abc}^R(\omega, -\omega) + \sigma_{acb}^R(\omega, -\omega)}{2} \\ &\quad + \frac{\sigma_{abc}^R(\omega, -\omega) - \sigma_{acb}^R(\omega, -\omega)}{2} \\ &= \sigma_{abc}^{\text{LDR}}(\omega, -\omega) + \sigma_{abc}^{\text{CDR}}(\omega, -\omega).\end{aligned}\quad (\text{B3})$$

Note that LDR/CDR indicates the linear/circular displacive Raman force. Considering the electric field in the xy -plane and for the case of CDR, we have

$$\mathcal{F}_a^{\text{CDR}} = \gamma_a^{\text{CDR}}(\omega)[i\mathbf{E}(\omega) \times \mathbf{E}^*(\omega)] \cdot \hat{\mathbf{z}}, \quad (\text{B4})$$

where the circular displacive Raman response function is given by

$$\gamma_a^{\text{CDR}}(\omega) = \frac{\sigma_{axy}^R(\omega, -\omega) - \sigma_{ayx}^R(\omega, -\omega)}{2i}. \quad (\text{B5})$$

The intrinsic permutation symmetry [85] implies that $\sigma_{ayx}^R(\omega, -\omega) = \sigma_{axy}^R(-\omega, \omega)$ and thus we obtain

$$\gamma_a^{\text{CDR}}(\omega) = \frac{\sigma_{axy}^R(\omega, -\omega) - \sigma_{axy}^R(-\omega, \omega)}{2i} = \text{Im}[\sigma_{axy}^R(\omega, -\omega)]. \quad (\text{B6})$$

Due to the reality of the electric field and the current, we have $\mathbf{E}^*(\omega) = \mathbf{E}(-\omega)$ and $[\sigma_{axy}^R(\omega, -\omega)]^* = \sigma_{axy}^R(-\omega, \omega)$. For the LDR, we find

$$\mathcal{F}_a^{\text{LDR}} = \gamma_{abc}^{\text{LDR}}(\omega)\text{Re}[E_b(\omega)E_c^*(\omega)]. \quad (\text{B7})$$

Using the permutation symmetry and the reality of current and electric field [85], we have $\sigma_{acb}^R(\omega, -\omega) = \sigma_{abc}^R(-\omega, \omega) = [\sigma_{abc}^R(\omega, -\omega)]^*$. Therefore, we obtain

$$\gamma_{abc}^{\text{LDR}}(\omega) = \frac{\sigma_{abc}^R(\omega, -\omega) + \sigma_{acb}^R(\omega, -\omega)}{2} = \text{Re}[\sigma_{abc}^R(\omega, -\omega)]. \quad (\text{B8})$$

APPENDIX C: RAMAN FORCE CALCULATION

The Raman response function to the external light electric field σ_{abc}^R is given in terms of χ_{abc}^R , which is the response to the vector potential

$$\sigma_{abc}^R(\omega_1, \omega_2) = -\frac{\chi_{abc}^R(\omega_1, \omega_2)}{\omega_1\omega_2}. \quad (\text{C1})$$

Here, we provide details of calculations for the Feynman diagrams given in Fig. 2 which stand for the $\chi_{abc}^R(\omega_1, \omega_2)$ response function. The total Raman response function is obtained as follows:

$$\begin{aligned}\chi_{abc}^R(\omega_1, \omega_2) &= \chi_{abc}^{\text{triangle}}(\omega_1, \omega_2) + \chi_{abc}^{\text{bubble-}\gamma}(\omega_1, \omega_2) \\ &\quad + \chi_{abc}^{\text{bubble-}\Theta}(\omega_1, \omega_2) + \chi_{abc}^{\text{bubble-}\Delta}.\end{aligned}\quad (\text{C2})$$

The contribution of photon-electron-phonon coupling Δ_{abc} depicted in the diagram in Fig. 2(d) is frequency-independent and therefore it can be fixed by enforcing the gauge

invariance that implies that a response to the static homogeneous gauge field must vanish due to the gauge invariance, i.e., $\chi_{abc}^R(\omega_1 = 0, \omega_2 = 0) = 0$. Since gauge invariance requires $\chi_{abc}^R(\omega_1 = 0, \omega_2 = 0) = 0$, we have

$$\begin{aligned}\chi_{abc}^{\text{bubble-}\Delta} &= -\chi_{abc}^{\text{triangle}}(0, 0) - \chi_{abc}^{\text{bubble-}\gamma}(0, 0) \\ &\quad - \chi_{abc}^{\text{bubble-}\Theta}(0, 0).\end{aligned}\quad (\text{C3})$$

Therefore, we find

$$\begin{aligned}\chi_{abc}^R(\omega_1, \omega_2) &= \bar{\chi}_{abc}^{\text{triangle}}(\omega_1, \omega_2) + \bar{\chi}_{abc}^{\text{bubble-}\gamma}(\omega_1, \omega_2) \\ &\quad + \bar{\chi}_{abc}^{\text{bubble-}\Theta}(\omega_1, \omega_2),\end{aligned}\quad (\text{C4})$$

in which we define $\bar{\chi}_{abc}(\omega_1, \omega_2) = \chi_{abc}(\omega_1, \omega_2) - \chi_{abc}(0, 0)$. In the following, we explicitly calculate these three remaining diagrams using the low-energy two-band model of bilayer graphene given in Eq. (5) and electron-phonon couplings Eq. (6).

1. Calculation of $\bar{\chi}_{abc}^{\text{triangle}}(\omega_1, \omega_2)$

The triangle diagram Fig. 2(a) can be written in terms of the electronic Green's function $\hat{G}(\mathbf{k}, ik_n)$ and the electron-phonon matrix-element \hat{M}_a and paramagnetic current operator \hat{j}_b, \hat{j}_c :

$$\begin{aligned}\chi_{abc}(i\omega_{m_1}, i\omega_{m_2}) &= \frac{1}{S} \sum_{\mathbf{k}} \frac{1}{\beta} \sum_{ik_n} \text{Tr}[\hat{M}_a(\mathbf{k})\hat{G}(\mathbf{k}, ik_n)\hat{j}_b(\mathbf{k}) \\ &\quad \times \hat{G}(\mathbf{k}, ik_n + i\omega_{m_1})\hat{j}_c(\mathbf{k})\hat{G}(\mathbf{k}, ik_n \\ &\quad + i\omega_{m_1} + i\omega_{m_2})],\end{aligned}\quad (\text{C5})$$

where the trace operator $\text{Tr}[\dots]$ sums over all spinor degree of freedom, $\beta = 1/k_B T_e$, and $ik_n (i\omega_m)$ stands for the fermionic (bosonic) Matsubara frequency. From now on, we adopt a shorthand notation $ik_n \rightarrow n$ and $i\omega_m \rightarrow m$ for the sake of simplicity. The electronic Green's function is given as follows:

$$\hat{G}(\mathbf{k}, ik_n) = [ik_n - \hat{H}_{\mathbf{k}}]^{-1}. \quad (\text{C6})$$

Because of the inversion symmetry, the Raman response tensor elements with odd Cartesian index x vanishes, $\chi_{xxx} = \chi_{yxy} = \chi_{xyy} = \chi_{yyx} = 0$, while those with odd Cartesian index y can be finite. This symmetry consideration is confirmed by an explicit calculation using the low-energy two-band Hamiltonian. The remaining tensor elements are also related to each other due to the rotation symmetry of the system:

$$\chi_{yyy} = \chi_{xxy} = \chi_{xyx} = -\chi_{yxx} = \chi_1. \quad (\text{C7})$$

It may seem counterintuitive to have a finite second-order response in an inversion-symmetric system. For instance, the second-order current response $j_a^{(2)} = \eta_{abc}^{(2)} E_b E_c$ vanishes due to the inversion symmetry, i.e., $\eta_{abc}^{(2)} = 0$. This is because the current operator is odd under parity, $\mathcal{P}\hat{j}_a\mathcal{P}^{-1} = -\hat{j}_a$. But the Raman-active phonon displacement field is even under parity as discussed in the main text, $\mathcal{P}Q_a\mathcal{P}^{-1} = Q_a$. Moreover, it

may seem nontrivial that χ_{abc} with an odd number of x index vanishes, but those with the odd number of y index are finite. We explain this issue within the low-energy model picture. Following Eqs. (8) and (9) at a given valley point (e.g., K valley), we find that \hat{M}_x evolves like a diamagnetic (two-photon) current vertex $\hat{\gamma}_{xy} = \hat{\gamma}_{yx} \sim \hat{\sigma}_y$. Therefore, the Raman response function $\chi_{xxx} \sim \langle \hat{M}_x \hat{J}_x \hat{J}_x \rangle$ is given in terms of a third-order current response function $\langle \hat{\gamma}_{xy} \hat{J}_x \hat{J}_x \rangle$, which consists of an odd number of x and y indices and thus it vanishes, $\chi_{xxx} = 0$, due

to inversion symmetry. On the other hand, we can see that \hat{M}_y evolves like $\hat{\gamma}_{xx} = -\hat{\gamma}_{yy} \sim \hat{\sigma}_x$ in the low-energy model, which implies $\chi_{yxx} \sim \langle \hat{M}_y \hat{J}_x \hat{J}_x \rangle$ evolves as the third-order current response function $\langle \hat{\gamma}_{xx} \hat{J}_x \hat{J}_x \rangle$. The latter consists of an even number of Cartesian index x , and thus it can be finite in an inversion-symmetric system. A similar argument can be used for other vanishing tensor elements of χ_{abc} .

After performing the integration on the azimuthal angle of electronic wave vector \mathbf{k} and using the low-energy dispersion $\epsilon_{\mathbf{k}} = \hbar^2 k^2 / 2m$ and $kdk = (m/\hbar^2)d\epsilon$, we find

$$\chi_1(m_1, m_2) = \left(\frac{N_f m M}{2\pi} \right) \left(\frac{e}{m} \right)^2 \left(\frac{m}{\hbar^2} \right) \int_0^\infty d\epsilon \frac{1}{\beta} \sum_n \times \frac{8\epsilon^2 \xi(n) \xi(m_1 + m_2 + n) [2\epsilon^2 - \xi(m_1 + n)^2 - \xi(m_2 + n)^2]}{[\epsilon^2 - \xi(n)^2][\epsilon^2 - \xi(m_1 + n)^2][\epsilon^2 - \xi(m_2 + n)^2][\epsilon^2 - \xi(m_1 + m_2 + n)^2]}, \quad (C8)$$

where $\xi(n) = \mu + n$. After performing Matsubara summation, integrating over ϵ at zero temperature, and then performing the analytical continuation $m_i \rightarrow \hbar\omega_i + i0^+$, we find

$$\chi_1(\omega_1, \omega_2) = \frac{N_f M e^2}{4\pi \hbar^2} \left\{ A_1 \ln [4\epsilon^2 - \omega_1^2] + A_2 \ln [4\epsilon^2 - \omega_2^2] + A_3 \ln [4\epsilon^2 - (\omega_1 + \omega_2)^2] \right\}_{\epsilon \rightarrow \mu}^{\epsilon \rightarrow \infty}. \quad (C9)$$

Here by ω_i we mean $\hbar\omega_i + i0^+$, and A_i factors explicitly read

$$A_1 = \frac{\omega_1(\omega_1 + 2\omega_2)}{\omega_2(\omega_1 + \omega_2)}, \quad A_2 = \frac{\omega_2(\omega_2 + 2\omega_1)}{\omega_1(\omega_1 + \omega_2)}, \quad A_3 = -\frac{(\omega_1 + \omega_2)^2}{\omega_1\omega_2} = -1 - (A_1 + A_2). \quad (C10)$$

By subtracting the zero-frequency contribution, and after some simplifications, we find

$$\chi_1(\omega_1, \omega_2) - \chi_1(0, 0) = \frac{N_f M e^2}{4\pi \hbar^2} \left\{ A_1 \ln \left[\frac{4\epsilon^2 - \omega_1^2}{4\epsilon^2 - (\omega_1 + \omega_2)^2} \right] + A_2 \ln \left[\frac{4\epsilon^2 - \omega_2^2}{4\epsilon^2 - (\omega_1 + \omega_2)^2} \right] - \ln \left[\frac{4\epsilon^2 - (\omega_1 + \omega_2)^2}{4\epsilon^2} \right] \right\}_{\epsilon \rightarrow \mu}^{\epsilon \rightarrow \infty}. \quad (C11)$$

Eventually, we obtain $\bar{\chi}_{yyy}^{\text{triangle}}(\omega_1, \omega_2) = \chi_1(\omega_1, \omega_2) - \chi_1(0, 0)$ as follows:

$$\bar{\chi}_{yyy}^{\text{triangle}}(\omega_1, \omega_2) = \frac{N_f M e^2}{4\pi \hbar^2} \left\{ \ln \left[1 - \frac{(\omega_1 + \omega_2)^2}{4\mu^2} \right] - A_1 \ln \left[\frac{4\mu^2 - \omega_1^2}{4\mu^2 - (\omega_1 + \omega_2)^2} \right] - A_2 \ln \left[\frac{4\mu^2 - \omega_2^2}{4\mu^2 - (\omega_1 + \omega_2)^2} \right] \right\}. \quad (C12)$$

2. Calculation of $\bar{\chi}_{abc}^{\text{bubble-}\gamma}(\omega_1, \omega_2)$

The bubble diagram in Fig. 2(b) can be written in terms of the electronic Green's function $\hat{G}(\mathbf{k}, n)$, the electron-phonon matrix-element \hat{M}_a , and the Raman vertex $\hat{\gamma}_{bc}$:

$$\chi_{abc}(m_1, m_2) = -\frac{1}{S} \sum_{\mathbf{k}} \frac{1}{\beta} \sum_n \text{Tr} [\hat{\mathcal{M}}_a^{(1)} \hat{G}(\mathbf{k}, n) \hat{\gamma}_{bc} \hat{G}(\mathbf{k}, n + m_1 + m_2)]. \quad (C13)$$

The over-all minus sign originates from the standard rules of Feynman diagrams [86]; also see [64]. Similar to the previous diagram, we have $\chi_{xxx} = \chi_{yxy} = \chi_{xyy} = \chi_{yyx} = 0$ by symmetry. The other nonvanishing tensor elements read

$$\chi_{yyy} = \chi_{xxy} = \chi_{xyx} = -\chi_{yxx} = \chi_2. \quad (C14)$$

After performing the integration on the azimuthal angle of the electronic wave vector \mathbf{k} and using the low-energy dispersion $\epsilon_{\mathbf{k}} = \hbar^2 k^2 / 2m$ and $kdk = (m/\hbar^2)d\epsilon$, we find

$$\chi_2(m_1, m_2) = \left(\frac{N_f M}{2\pi} \right) \frac{e^2 m}{m \hbar^2} \int_0^\infty d\epsilon \frac{1}{\beta} \sum_n \frac{2\xi(n)\xi(m_1 + m_2 + n)}{[\epsilon^2 - \xi(n)^2][\epsilon^2 - \xi(m_1 + m_2 + n)^2]}. \quad (C15)$$

After performing the summation on the Matsubara frequency n and subtracting the zero-frequency contribution, we find

$$\chi_2(\omega_1, \omega_2) - \chi_2(0, 0) = -\frac{N_f M e^2}{8\pi \hbar^2} \left\{ \ln \left[\frac{4\epsilon^2 - (\omega_1 + \omega_2)^2}{4\epsilon^2} \right] \right\}_{\epsilon \rightarrow \mu}^{\epsilon \rightarrow \infty}. \quad (C16)$$

Finally, we obtain

$$\bar{\chi}_{yyy}^{\text{bubble}-\gamma}(\omega_1, \omega_2) = \frac{N_f M e^2}{8\pi \hbar^2} \ln \left[1 - \frac{(\omega_1 + \omega_2)^2}{4\mu^2} \right]. \quad (\text{C17})$$

3. Calculation of $\bar{\chi}_{abc}^{\text{bubble}-\Theta}(\omega_1, \omega_2)$

The bubble diagram in Fig. 2(c) can be written in terms of the electronic Green's function $\hat{G}(\mathbf{k}, n)$, the photon-electron-phonon vertex $\hat{\Theta}_{ab}$, and the paramagnetic current \hat{j}_c . Considering the permutation symmetry, we have

$$\begin{aligned} \chi_{abc}(m_1, m_2) = & -\frac{1}{2S} \sum_{\mathbf{k}} \frac{1}{\beta} \sum_n \text{Tr}[\hat{\Theta}_{ab} \hat{G}(\mathbf{k}, n) \hat{j}_c(\mathbf{k}) \hat{G}(\mathbf{k}, n + m_2)] \\ & - \frac{1}{2S} \sum_{\mathbf{k}} \frac{1}{\beta} \sum_n \text{Tr}[\hat{\Theta}_{ac} \hat{G}(\mathbf{k}, n) \hat{j}_b(\mathbf{k}) \hat{G}(\mathbf{k}, n + m_1)]. \end{aligned} \quad (\text{C18})$$

Using the isotropic approximation for the photon-electron-phonon vertex given in Eq. (6) and after performing the integration on the azimuthal angle of electronic wave vector \mathbf{k} , we obtain a vanishing result for all tensor elements. Therefore, within our low-energy model analysis, the mix photon-electron-phonon coupling does not contribute to the Raman force:

$$\bar{\chi}_{abc}^{\text{bubble}-\Theta}(\omega_1, \omega_2) = 0. \quad (\text{C19})$$

APPENDIX D: FINITE ELECTRONIC TEMPERATURE T_e EFFECT

At finite electronic temperature, we first need to calculate the temperature dependence of the chemical potential. Using the isotropic two-band model of bilayer graphene, we can easily show that the chemical potential is equal to the Fermi energy: $\mu = \epsilon_F$ [87]. We summarize this derivation as follows: The total charge density is given in terms of electron and hole density $-en = -e|n_e - n_h|$, where

$$\begin{aligned} n = & \frac{N_f}{S} \sum_p [n_F(\epsilon_p) + n_F(-\epsilon_p) - 1] = \frac{N_f m k_B T_e}{2\pi \hbar^2} \\ & \times \int_0^\infty dx \left\{ \frac{1}{1 + e^{x - \frac{\mu}{k_B T_e}}} - \frac{1}{1 + e^{x + \frac{\mu}{k_B T_e}}} \right\} = \frac{2m\epsilon_F}{\pi \hbar^2}. \end{aligned} \quad (\text{D1})$$

Note that we have used $\epsilon_p = p^2/2m$. We can simplify the above relation as follows:

$$\frac{\epsilon_F}{k_B T_e} = \int_0^\infty dx \left\{ \frac{1}{1 + e^{x - \frac{\mu}{k_B T_e}}} - \frac{1}{1 + e^{x + \frac{\mu}{k_B T_e}}} \right\}, \quad (\text{D2})$$

and thus we find

$$\frac{\epsilon_F}{k_B T_e} = \ln[1 + e^{\frac{\mu}{k_B T_e}}] - \ln[1 + e^{\frac{-\mu}{k_B T_e}}]. \quad (\text{D3})$$

One can quickly solve the above relation and find $\mu = \epsilon_F$. For finite electronic temperature T_e , we can utilize the following identity [88]:

$$\frac{1}{e^x + 1} = \int_{-\infty}^\infty \frac{\Theta(y - x)}{4 \cosh^2(y/2)} dy, \quad (\text{D4})$$

where $\Theta(x)$ is the Heaviside step function. Using the above identity, we calculate the finite-temperature response function by integrating over the zero-temperature one. Accordingly, we replace $\ell_n(z, \mu) = |\mu|^n \ln[(z - 2|\mu|)/(z + 2|\mu|)]$ with $L_n(z, \mu, T)$ and we numerically solve the integration:

$$L_n(z, \mu, T_e) = \int_{-\infty}^{+\infty} dx \frac{\ell_n(z, x)}{4k_B T_e \cosh^2\left(\frac{x - \mu}{2k_B T_e}\right)}. \quad (\text{D5})$$

-
- [1] J. M. B. Lopes dos Santos, N. M. R. Peres, and A. H. Castro Neto, *Phys. Rev. Lett.* **99**, 256802 (2007).
[2] J. H. Ho, C. L. Lu, C. C. Hwang, C. P. Chang, and M. F. Lin, *Phys. Rev. B* **74**, 085406 (2006).
[3] C. J. Tabert and E. J. Nicol, *Phys. Rev. B* **86**, 075439 (2012).
[4] R. Bistritzer and A. H. MacDonald, *Proc. Natl. Acad. Sci. USA* **108**, 12233 (2011).
[5] J. M. B. Lopes dos Santos, N. M. R. Peres, and A. H. Castro Neto, *Phys. Rev. B* **86**, 155449 (2012).
[6] A. L. Rakhmanov, A. V. Rozhkov, A. O. Sboychakov, and F. Nori, *Phys. Rev. Lett.* **109**, 206801 (2012).
[7] E. McCann and M. Koshino, *Rep. Prog. Phys.* **76**, 056503 (2013).
[8] R. Roldán and L. Brey, *Phys. Rev. B* **88**, 115420 (2013).
[9] M. Koshino and E. McCann, *Phys. Rev. B* **79**, 125443 (2009).
[10] A. A. Avetisyan, B. Partoens, and F. M. Peeters, *Phys. Rev. B* **79**, 035421 (2009).
[11] A. A. Avetisyan, B. Partoens, and F. M. Peeters, *Phys. Rev. B* **81**, 115432 (2010).
[12] X. Li, F. Wu, and A. H. MacDonald, *arXiv:1907.12338*.
[13] C. Mora, N. Regnault, and B. A. Bernevig, *Phys. Rev. Lett.* **123**, 026402 (2019).
[14] V. O. T. Phong, P. A. Pantaleón, T. Cea, and F. Guinea, *Phys. Rev. B* **104**, L121116 (2021).
[15] W. Qin and A. H. MacDonald, *Phys. Rev. Lett.* **127**, 097001 (2021).

- [16] H. C. Po, L. Zou, A. Vishwanath, and T. Senthil, *Phys. Rev. X* **8**, 031089 (2018).
- [17] L. Zou, H. C. Po, A. Vishwanath, and T. Senthil, *Phys. Rev. B* **98**, 085435 (2018).
- [18] M. Angeli, D. Mandelli, A. Valli, A. Amaricci, M. Capone, E. Tosatti, and M. Fabrizio, *Phys. Rev. B* **98**, 235137 (2018).
- [19] M. Koshino, N. F. Q. Yuan, T. Koretsune, M. Ochi, K. Kuroki, and L. Fu, *Phys. Rev. X* **8**, 031087 (2018).
- [20] J. Kang and O. Vafek, *Phys. Rev. X* **8**, 031088 (2018).
- [21] Y. Cao, V. Fatemi, S. Fang, K. Watanabe, T. Taniguchi, E. Kaxiras, and P. Jarillo-Herrero, *Nature (London)* **556**, 43 (2018).
- [22] Y. Cao, V. Fatemi, A. Demir, S. Fang, S. L. Tomarken, J. Y. Luo, J. D. Sanchez-Yamagishi, K. Watanabe, T. Taniguchi, E. Kaxiras, R. C. Ashoori, and P. Jarillo-Herrero, *Nature (London)* **556**, 80 (2018).
- [23] Z. Zhu, S. Carr, D. Massatt, M. Luskin, and E. Kaxiras, *Phys. Rev. Lett.* **125**, 116404 (2020).
- [24] C. Lei, L. Linhart, W. Qin, F. Libisch, and A. H. MacDonald, *Phys. Rev. B* **104**, 035139 (2021).
- [25] P. H. Tan, W. P. Han, W. J. Zhao, Z. H. Wu, K. Chang, H. Wang, Y. F. Wang, N. Bonini, N. Marzari, N. Pugno, G. Savini, A. Lombardo, and A. C. Ferrari, *Nat. Mater.* **11**, 294 (2012).
- [26] A. C. Ferrari and D. M. Basko, *Nat. Nanotechnol.* **8**, 235 (2013).
- [27] X. Zhang, W. P. Han, J. B. Wu, S. Milana, Y. Lu, Q. Q. Li, A. C. Ferrari, and P. H. Tan, *Phys. Rev. B* **87**, 115413 (2013).
- [28] H. Zeng, B. Zhu, K. Liu, J. Fan, X. Cui, and Q. M. Zhang, *Phys. Rev. B* **86**, 241301(R) (2012).
- [29] K. H. Michel and B. Verberck, *Phys. Rev. B* **78**, 085424 (2008).
- [30] K. H. Michel and B. Verberck, *Phys. Rev. B* **85**, 094303 (2012).
- [31] Y. Zhao, X. Luo, H. Li, J. Zhang, P. T. Araujo, C. K. Gan, J. Wu, H. Zhang, S. Y. Quek, M. S. Dresselhaus, and Q. Xiong, *Nano Lett.* **13**, 1007 (2013).
- [32] G. Wang, X. Li, Y. Wang, Z. Zheng, Z. Dai, X. Qi, L. Liu, Z. Cheng, Z. Xu, P. Tan, and Z. Zhang, *J. Phys. Chem. C* **121**, 26034 (2017).
- [33] G. Pizzi, S. Milana, A. C. Ferrari, N. Marzari, and M. Gibertini, *ACS Nano* **15**, 12509 (2021).
- [34] M. S. Dresselhaus, G. Dresselhaus, and A. Jorio, *Group Theory: Application to the Physics of Condensed Matter* (Springer Science & Business Media, Berlin, 2007).
- [35] P. Yu and M. Cardona, *Fundamentals of Semiconductors: Physics and Materials Properties*, Graduate Texts in Physics (Springer, Berlin, 2010).
- [36] J. Zhang, J. Han, G. Peng, X. Yang, X. Yuan, Y. Li, J. Chen, W. Xu, K. Liu, Z. Zhu, W. Cao, Z. Han, J. Dai, M. Zhu, S. Qin, and K. S. Novoselov, *Light Sci. Appl.* **9**, 174 (2020).
- [37] E. J. Sie, C. M. Nyby, C. D. Pemmaraju, S. J. Park, X. Shen, J. Yang, M. C. Hoffmann, B. K. Ofori-Okai, R. Li, A. H. Reid, S. Weathersby, E. Mannebach, N. Finney, D. Rhodes, D. Chenet, A. Antony, L. Balicas, J. Hone, T. P. Devereaux, T. F. Heinz, X. Wang, and A. M. Lindenberg, *Nature (London)* **565**, 61 (2019).
- [38] M. Y. Zhang, Z. X. Wang, Y. N. Li, L. Y. Shi, D. Wu, T. Lin, S. J. Zhang, Y. Q. Liu, Q. M. Liu, J. Wang, T. Dong, and N. L. Wang, *Phys. Rev. X* **9**, 021036 (2019).
- [39] T. Fukuda, K. Makino, Y. Saito, P. Fons, A. V. Kolobov, K. Ueno, and M. Hase, *Appl. Phys. Lett.* **116**, 093103 (2020).
- [40] S. Ji, O. Grånäs, and J. Weissenrieder, *ACS Nano* **15**, 8826 (2021).
- [41] Z. Zheng, Q. Ma, Z. Bi, S. de la Barrera, M.-H. Liu, N. Mao, Y. Zhang, N. Kiper, K. Watanabe, T. Taniguchi, J. Kong, W. A. Tisdale, R. Ashoori, N. Gedik, L. Fu, S.-Y. Xu, and P. Jarillo-Herrero, *Nature (London)* **588**, 71 (2020).
- [42] C. R. Woods, P. Ares, H. Nevison-Andrews, M. J. Holwill, R. Fabregas, F. Guinea, A. K. Geim, K. S. Novoselov, N. R. Walet, and L. Fumagalli, *Nat. Commun.* **12**, 347 (2021).
- [43] Y. Kenji, W. Xirui, W. Kenji, T. Takashi, and J.-H. Pablo, *Science* **372**, 1458 (2021).
- [44] M. V. Stern, Y. Waschitz, W. Cao, I. Nevo, K. Watanabe, T. Taniguchi, E. Sela, M. Urbakh, O. Hod, and M. Ben Shalom, *Science* **372**, 1462 (2021).
- [45] Z. Fei, W. Zhao, T. A. Palomaki, B. Sun, M. K. Miller, Z. Zhao, J. Yan, X. Xu, and D. H. Cobden, *Nature (London)* **560**, 336 (2018).
- [46] P. Sharma, F.-X. Xiang, D.-F. Shao, D. Zhang, E. Y. Tsymbal, A. R. Hamilton, and Jan Seidel, *Sci. Adv.* **5**, eaax5080 (2019).
- [47] W. X. Zhou and A. Ariando, *Jpn. J. Appl. Phys.* **59**, SI0802 (2020).
- [48] A. S. Disa, T. F. Nova, and A. Cavalleri, *Nat. Phys.* **17**, 1087 (2021).
- [49] J. G. Horstmann, H. Böckmann, B. Wit, F. Kurtz, G. Storeck, and C. Ropers, *Nature (London)* **583**, 232 (2020).
- [50] M. Born, K. Huang, and M. Lax, *Am. J. Phys.* **23**, 474 (1955).
- [51] G. Lanzani, G. Cerullo, and S. De Silvestri, *Coherent Vibrational Dynamics* (CRC, Boca Raton, FL, 2007).
- [52] T. Dekorsy, G. C. Cho, and H. Kurz, Coherent phonons in condensed media, in *Light Scattering in Solids VIII: Fullerenes, Semiconductor Surfaces, Coherent Phonons*, edited by M. Cardona and G. Güntherodt (Springer, Berlin, 2000), pp. 169–209.
- [53] M. Hase, M. Kitajima, A. M. Constantinescu, and H. Petek, *Nature (London)* **426**, 51 (2003).
- [54] K. Ishioka, M. Hase, M. Kitajima, and H. Petek, *Appl. Phys. Lett.* **89**, 231916 (2006).
- [55] H. J. Zeiger, J. Vidal, T. K. Cheng, E. P. Ippen, G. Dresselhaus, and M. S. Dresselhaus, *Phys. Rev. B* **45**, 768 (1992).
- [56] T. Pfeifer, T. Dekorsy, W. Kütt, and H. Kurz, *Appl. Phys. A* **55**, 482 (1992).
- [57] A. V. Kuznetsov and C. J. Stanton, *Phys. Rev. Lett.* **73**, 3243 (1994).
- [58] A. V. Kuznetsov and C. J. Stanton, *Phys. Rev. B* **51**, 7555 (1995).
- [59] T. E. Stevens, J. Kuhl, and R. Merlin, *Phys. Rev. B* **65**, 144304 (2002).
- [60] G. A. Garrett, T. F. Albrecht, J. F. Whitaker, and R. Merlin, *Phys. Rev. Lett.* **77**, 3661 (1996).
- [61] R. Merlin, *Solid State Commun.* **102**, 207 (1997).
- [62] For the shear phonon in bilayer graphene, the zero-order force in the absence of the light pulse vanishes due to the particular spinor structure of the electron-phonon matrix element given in Eq. (9).
- [63] T. P. Devereaux and R. Hackl, *Rev. Mod. Phys.* **79**, 175 (2007).
- [64] H. Rostami, M. I. Katsnelson, G. Vignale, and M. Polini, *Ann. Phys.* **431**, 168523 (2021).
- [65] H. Rostami and E. Cappelluti, *npj 2D Mater. Appl.* **5**, 50 (2021).
- [66] E. Cappelluti, L. Benfatto, M. Manzardo, and A. B. Kuzmenko, *Phys. Rev. B* **86**, 115439 (2012).
- [67] T. Cea and L. Benfatto, *Phys. Rev. B* **90**, 224515 (2014).

- [68] E. McCann and V. I. Fal'ko, *Phys. Rev. Lett.* **96**, 086805 (2006).
- [69] H. Rostami and R. Asgari, *Phys. Rev. B* **88**, 035404 (2013).
- [70] K. Ishikawa and T. Ando, *J. Phys. Soc. Jpn.* **75**, 084713 (2006).
- [71] E. Cappelluti and G. Profeta, *Phys. Rev. B* **85**, 205436 (2012).
- [72] D. M. Basko, *New J. Phys.* **11**, 095011 (2009).
- [73] V. I. Belinicher and B. I. Sturman, *Sov. Phys. Usp.* **23**, 199 (1980).
- [74] C. H. Lui, K. F. Mak, J. Shan, and T. F. Heinz, *Phys. Rev. Lett.* **105**, 127404 (2010).
- [75] A. Tomadin, D. Brida, G. Cerullo, A. C. Ferrari, and M. Polini, *Phys. Rev. B* **88**, 035430 (2013).
- [76] D. Brida, A. Tomadin, C. Manzoni, Y. J. Kim, A. Lombardo, S. Milana, R. R. Nair, K. S. Novoselov, A. C. Ferrari, G. Cerullo, and M. Polini, *Nat. Commun.* **4**, 1987 (2013).
- [77] A. Tomadin, S. M. Hornett, H. I. Wang, E. M. Alexeev, A. Candini, C. Coletti, D. Turchinovich, M. Kläui, M. Bonn, F. H. L. Koppens, E. Hendry, M. Polini, and K.-J. Tielrooij, *Sci. Adv.* **4**, eaar5313 (2018).
- [78] F. Andreatta, H. Rostami, A. G. Cabo, M. Bianchi, C. E. Sanders, D. Biswas, C. Cacho, A. J. H. Jones, R. T. Chapman, E. Springate, P. D. C. King, J. A. Miwa, A. Balatsky, S. Ulstrup, and P. Hofmann, *Phys. Rev. B* **99**, 165421 (2019).
- [79] A. T. Roberts, R. Binder, N. H. Kwong, D. Golla, D. Cormode, B. J. LeRoy, H. O. Everitt, and A. Sandhu, *Phys. Rev. Lett.* **112**, 187401 (2014).
- [80] D. Novko and M. Kralj, *npj 2D Mater. Appl.* **3**, 48 (2019).
- [81] E. Cappelluti, F. Caruso, and D. Novko, *Prog. Surf. Sci.* **97**, 100664 (2022).
- [82] M. B. Silva Neto and L. Benfatto, *Phys. Rev. B* **72**, 140401(R) (2005).
- [83] L. Zhang and Q. Niu, *Phys. Rev. Lett.* **115**, 115502 (2015).
- [84] H. Rostami, F. Guinea, and E. Cappelluti, *Phys. Rev. B* **105**, 195431 (2022).
- [85] P. Butcher and D. Cotter, *The Elements of Nonlinear Optics* (Cambridge University Press, Cambridge, 1990).
- [86] G. D. Mahan, *Many-Particle Physics* (Springer, US, New York, 1995).
- [87] S. Adam and M. D. Stiles, *Phys. Rev. B* **82**, 075423 (2010).
- [88] G. Giuliani and G. Vignale, *Quantum Theory of the Electron Liquid* (Cambridge University Press, Cambridge, 2005).